# EXPERIMENTAL INVESTIGATION OF THE INFLUENCE OF INJECTION PRESSURE AND CLAY SMEAR ON FAULT REACTIVATION FOR $CO_2$ STORAGE

**Luke Griffiths*[1], Joonsang Park[1], Pierre Cerasi[2], Laura Edvardsen[2], Andreas Wüstefeld[3]**

[1] NGI - Norwegian Geotechnical Institute, Oslo, Norway

[2] SINTEF Industry, Trondheim, Norway

[3] NORSAR, Kjeller, Norway

* Corresponding author e-mail: luke.griffiths@ngi.no

## Abstract

## Abstract

Induced microseismicity from subsurface engineering projects such as geothermal heat exploitation and $CO_2$ storage can be a show-stopper and halt the development of a site. While microseismicity correlates with fluid injection in the ground, the magnitudes of events are difficult to predict and some faults in the underground release significant energy, while others do not. Here, we test in the laboratory the hypothesis that clay content in the fault gouge may dampen asperity breakage upon shear slip and explain why certain faults release less elastic energy. We performed two triaxial tests on a sample of Castlegate sandstone to simulate fault reactivation as a result of pore pressure increase due to $CO_2$ (or water) injection, whilst measuring axial and radial P-wave velocities and monitoring acoustic emissions (AE; laboratory scale microseismicity). A through-going fracture was created by axial loading of the sample to failure. The axial stress was then reduced to 80% of the residual strength of the sample, and the fracture was reactivated by pore pressure pulses at rates of 3, 6, 12 and 24 MPa/hr. Although no $CO_2$ or second phase fluid was injected, the pressure pulse simulates the pressure propagation ahead of the injected fluid. Following the test, the sample was separated along the fracture plane, and the fracture was filled with a clay (kaolinite) gouge, reassembled, and the test procedure was repeated. For both tests we analysed AE locations, rate, and magnitude distribution, and determined source mechanisms. AE during the first test on the intact sample occurred throughout the sample during axial loading until coalescing along the macroscopic fault plane observed using 3D CT imaging. AE during the reactivation stages were located predominantly along the fracture. For the clean fracture, the pore pressure increase rate had no clear effect on the pressure for reactivation, i.e., no weakening at higher injection rates. For the sample containing a clay-filled fracture, we observed very little AE activity during all test stages and we were unable to reach stable sliding of the in-filled fracture during axial loading as for the clean fracture. We observed a slight increase in the pore pressure reactivation pressure at higher pressurisation rates which we attribute to plastic deformation of the fault gouge. These results suggest that, for the pressurisation rates observed, $CO_2$ injection rates may only have a negligible effect on fault stability, which is controlled rather by the absolute pressure changes.

***Keywords:*** *$CO_2$ reservoir, sandstone, fault, clay smear, microseismicity*

## 1. Introduction

Carbon capture and storage (CCS) could play an essential role in meeting net-zero global $CO_2$ emission [1]. Currently, North Sea saline aquifers are targets for large-scale geological storage of $CO_2$. At such storage sites, pressure changes due to $CO_2$ injection may cause undesired deformation, and even slip on faults within and around the reservoir [2]. This could produce permeable pathways for fluid migration towards the surface, as well as microseismic activity. An assessment of the risk of leakage of $CO_2$ to the seabed requires a deep understanding of the mechanical properties of the reservoir and the potential for fracturing or reactivation of existing fractures and faults [3]. Specifically, it is important to know the influence of $CO_2$ injection rate translated into pore pressure increase on fault instability to develop an injection strategy to prevent, and limit, microseismicity and potential for leakage. If better understood, microseismicity could be employed as a monitoring tool; this presupposes that one has the means to keep magnitudes below levels felt by humans on the ground (and obviously below levels capable of causing structural damage in built-up areas). The assumption is that microseismicity could monitor the pressure plume preceding the injected $CO_2$ fluid plume, and thus give an early warning on lack of conformance with predictions.

To better understand the influence of pressurisation rate on fault reactivation within reservoir sandstone, mechanical testing may be performed under controlled fluid saturation and stress conditions in the laboratory. When deforming rock samples in the laboratory, the macroscopic stress state is known and, through monitoring the laboratory-scale microseismic events (or Acoustic Emissions: AE), the initiation and location of any failure plane can be monitored as it develops. AE monitoring is a well-established technique to study failure processes in rocks [4]–[9].

In this study, we performed two triaxial tests on a sandstone sample relevant to North Sea CCS. First, we created a through-going fracture within the sample by axial loading at a constant axial deformation rate, which was then reactivated by pore pressure pulses at different rates. The sample was separated along the fracture and the fracture was filled with a clay gouge. The sample was then reassembled, and the test was repeated. We compare the mechanical and microseismic response of the samples to reactivation of the fracture through axial deformation, and then by pore pressure increase at different rates.

## 2. Materials and methods

### *2.1 Materials*

Castlegate sandstone was selected for this study as it is a relatively homogeneous, clay-free rock, and has previously been used as part of a study on fracture reactivation by pore pressure increase [10]. The sandstone sample was a cylinder of 119.85 mm in length and 49.815 mm in diameter. Two tests were performed on the same sample. Test 1 was performed on the initially intact sample (Figure 1a), where a through-going fracture was created by axial loading, and the fracture was reactivated by pore pressure increase at different rates. In Test 2 the same sample was used, but with kaolin spread along the fracture (Figure 1b) as an analogue to clay-smear along a fault.

### *2.2 Testing equipment*

Tests were performed within a triaxial apparatus at NGI (schematic shown in Figure 1c; [4], [11]) which can independently control the axial (vertical) and radial (horizontal or confining) stresses and the pressure of the pore fluid within the rock. The sample is held between two platens through which pore fluid may be injected. Steel filters between each end of the sample and the pistons prevent particles from entering the pore line tubing and ensure pressure is evenly distributed across the sample faces. The sample is contained within a nitrile sleeve to isolate it from the confining oil. Axial deformation is measured using two LVDTs mounted to the top and bottom platens (Figure 1c). The radial deformation is measured using strain gauges attached to a cantilever, fixed directly to the sample mid-height via 4 pins. The axial load (via a pressure chamber above the upper piston), confining pressure, and pore pressure are controlled by GDS pumps. The initial consolidation stresses were chosen to be the same as used by Cerasi et al. (2018) on samples of the same material: 5 MPa total isotropic stress and 2 MPa pore pressure.

Ultrasonic P-wave velocities in the axial and radial directions were measured during the tests at regular intervals through pairs of piezo transducers embedded within the platens and at the sample mid-height (Figure 2). AE monitoring was performed using 12 piezoelectric transducers (pinducers from Ergotech Ltd, UK), sensitive to displacement, and attached through the jacket to the lateral surface of the sample (Figure 1c). The transducers have a resonant frequency of around 1MHz, with most energy centered on 0.5 MHz [4]. The Milne acquisition system (Itasca Consulting, UK) is used to record waveforms during velocity measurements and detect and record AE events. An event is recorded when the trigger voltage is surpassed at more than 4 of the 16 sensors (12 pinducers and 4 piezo-transducers). We recorded waveforms at 10 MHz sampling rate and 12-bit amplitude resolution, over durations of 409.5 µs. Waveforms recorded through AE monitoring and active surveys were filtered using a band-pass filter with 10 kHz low-cut and 1 MHz high-cut frequencies.

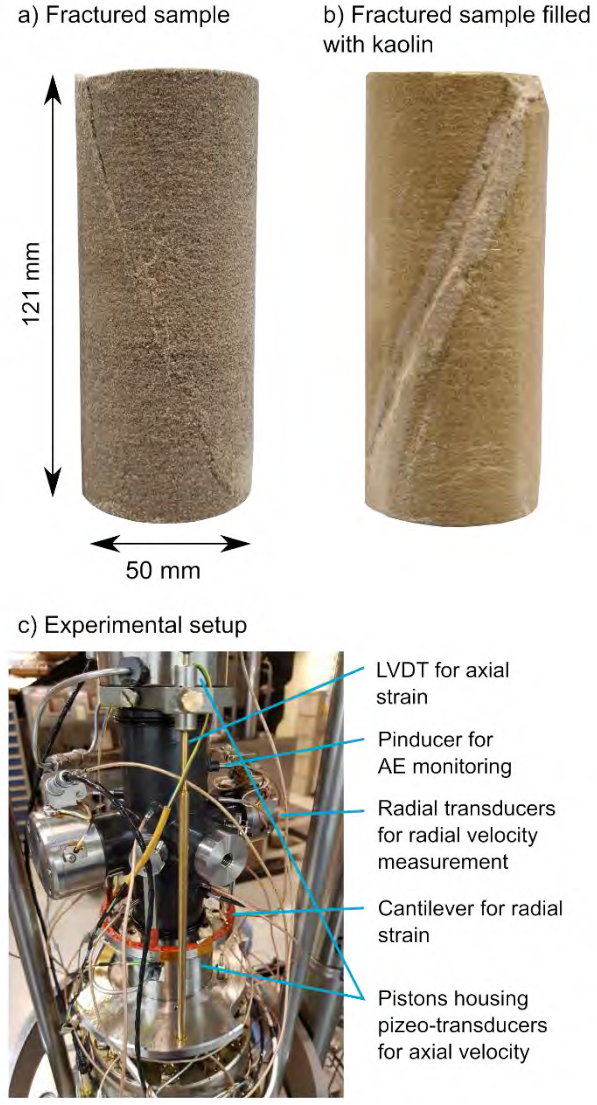


Figure 1: (a) The fractured sample following Test 1. (b) The same sample is used for Test 2 but with kaolin filling the through-going fracture. (c) The jacketed sample and instrumented sample within the triaxial apparatus.

To calibrate the voltage amplitudes at each sensor, we recorded across all 16 channels several pulses emitted from the larger axial and radial sensor pairs used for the velocity surveys (Figure 1c). The voltages at each of the 16 sensors were then scaled by a multiplicative factor so that each sensor gave the same relative "location magnitude" for the pulses, relative to a reference sensor. The relative magnitude (m) is given by equation (1), in the case where voltages at multiple ($N$) sensors are considered, $V_{RMS}$ is the RMS voltage, and $d_m$ is the distance between the event and the receiver (from Pettitt

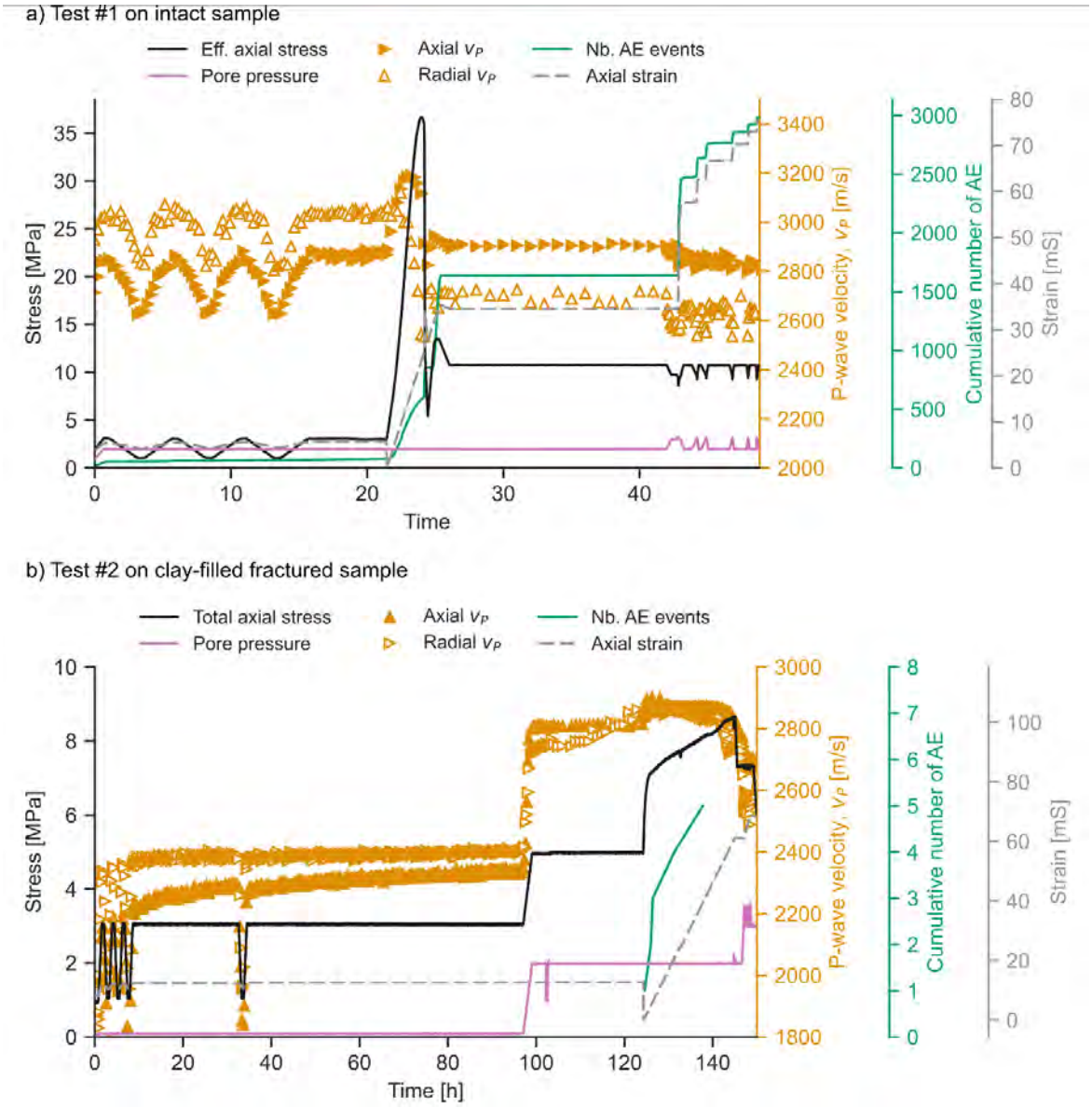


Figure 2: Timelines for triaxial tests on Castlegate sandstone: (a) Test on an initially intact sample; (b) test on the same sample, with kaolinite along the fracture.

and Young (2007)). The calibration waveforms were acquired at the consolidation stresses prior to shearing. Measurements were made for multiple pulses from each sensor to verify the consistency of the voltage signals. The calibration highlighted a greater sensitivity of the sensors located within the platen compared to the smaller radial sensors. We therefore excluded the sensors within the platens from the location and source mechanism calculation to avoid any bias.

$$m = \log_{10}\left(\frac{\sum_{m=1}^{N} V_{RMS}.d_m}{N}\right) \qquad (1)$$

### *2.3 Stress paths*

#### *2.3.1. Sandstone containing clean fracture*

Figure 2a depicts a timeline of Test 1 on the initially intact Castlegate sandstone sample. The sample was first held under vacuum and pressurized to 1 MPa confining pressure. Brine (35g/L NaCl) was then allowed to enter the sample, and the pore pressure was increased to 0.1 MPa. AE trigger thresholds were adjusted for each sensor to be just above the noise level of the equipment and velocity surveys were scheduled every 15 minutes. The cell pressure was increased to 5 MPa and the pore pressure to 2 MPa over 70 minutes. Cell pressure was cycled from 5 to 3 MPa at 1 MPa/hr (three cycles), with 30 min between ramps to allow for stabilization of strain due to any adjustment of the sample and the loading frame.

To create a through-going fracture, the sample was axially deformed at a constant strain rate of 3 mS/hr to beyond the peak stress (26.6 MPa effective axial stress), until the axial stress had stabilized at the residual strength of the fractured sample (13.5 MPa effective axial stress; Figure 2a). The axial stress was then decreased to 80 % of the of residual stress (10.8 MPa) at a rate of 3.75 MPa/hr.

The fracture was then reactivated multiple times by increasing pore pressure from 2 MPa at 3 MPa/hr. The pore pressure was increased until we observed an acceleration of the axial strain as the fracture began to slip (giving the pore pressure reactivation pressure), at which point we then decreased the pore pressure to 2 MPa at the same rate. Reactivation at 2 MPa/hr was repeated three times at rates of 6, 12 and 24 MPa/hr, unloading at reactivation to 2 MPa in 7 minutes (~10 MPa/hr). Finally, the axial stress was unloaded at 3.75 MPa/hr to isotropic conditions and the sample was removed from the cell.

*2.3.2. Sandstone containing clean fracture*

Test 2 was performed on the same sample as used in Test 1. Prior to testing, the sample was separated into two pieces when wet, and dried in an oven for 48 hr (mass change between 24 and 48 hours was 0.02-0.04 g). Kaolin (Speswhite™) mixed with distilled water was applied to each side of the fracture, resulting in a coating with 1-2 mm thickness (Figure 1c). X-ray micro-computed tomography (µ-CT) was used to assess the coverage of the clay within the fracture, which was found to be continuous across the fracture surface, and completely filling the fracture aperture.

The sample was then placed within the nitrile jacket with the same orientation as during Test 1. As for Test 1, the sample was pressurised to 1 MPa confining pressure and saturated with 35 g/L NaCl brine. The AE trigger thresholds were individually adjusted to just above the noise level. Cell pressure was increased to 5 MPa and pore pressure to 2 MPa. The cell pressure was decreased from 5 to 3 MPa and back, at a rate of 1 MPa/hr (three times), with 30 min between ramps. Following a period of 24 hours at the consolidation stresses, the cell pressure was cycled again at the same rate, to see whether there were any long-term changes in the mechanical properties of the sample in presence of clay (which there were not).

Axial stress was increased to deform the sample at a constant strain rate of 3 mS/hr. We expected the stress to reach a peak value and stabilize at the residual strength of the fracture, as for Test 1. Instead, the axial stress continued to increase within the deformation range of the test, and the axial loading was stopped at an arbitrary value of 7.3 MPa effective axial stress. The effective axial stress was then decreased to 80 % of this value: 5.3 MPa, at which stress the axial and radial strain remained stable.

The clay-filled fracture was reactivated multiple times by increasing the pore pressure at rates of 3 MPa/h (three times), and 6, 12, and 24 MPa/hr (one time) until an acceleration of the axial strain was observed (at the pore pressure reactivation pressure). Finally, the axial stress was unloaded at 3.75 MPa/hr to isotropic conditions and the sample was removed from the cell.

## 3. Results

### *3.1 Fracture reactivation*

Table 1 gives the fracture reactivation pore pressure for the different rates of pore pressure increase used in Tests 1 and 2. The fracture reactivation pressures were determined at the onset of slip by an increase in axial deformation and drop in axial stress. For Test 1 the initial fracture reactivation had the highest reactivation pressure at 3.27 MPa, compared to around 3.1 MPa for all subsequent reactivations, regardless of the rate of increasing pore pressure. For Test 2 a slight increase in reactivation pressure with pore pressure increase rate was observed: from 3.21 MPa for the first reactivation at 3 MPa/hr, to 3.39 MPa for the final reactivation at 24 MPa/hr (Table 1). We note, however, that the overall influence of pore pressure increase rate on the absolute reactivation pressure was low.

Table 1: Pore pressures for fracture reactivation for different pore pressure increase rates for Test 1 on a "clean" fractured sandstone, and Test 2 on fractured sandstone with clay fault.

| Test | Cell pressure [MPa] | Axial stress [MPa] | Initial pore pressure [MPa] | Pore pressure increase rate [MPa/hour] | Pore pressure reactivation pressure [MPa] |
|---|---|---|---|---|---|
| 1 | 5 | 10.8 | 3 | 3 | 3.27 |
| | | | 2 | 2 | 3.07 |
| | | | | 3 | 3.08 |
| | | | | 6 | 3.12 |
| | | | | 12 | 3.14 |
| | | | | 24 | 3.1 |
| 2 | 5 | 7.3 | 2 | 3 | 3.21 |
| | | | 3 | 3 | 3.3 |
| | | | | 3 | 3.28 |
| | | | | 6 | 3.31 |
| | | | | 12 | 3.35 |
| | | | | 24 | 3.39 |

### *3.2 Passive and active acoustic monitoring*

*3.2.1 P-wave velocities and AE locations*

Figure 2a shows the P-wave velocities in the radial (at the sample mid-height) and axial directions, calculated from the P-wave travel times between opposing source-receiver pairs and the sample dimensions (accounting for sample deformation).

Also shown in Figure 2 are the number of located AE during each test. For Test 1 (Figure 2a), across all test phases, a total of 2904 AE events were detected, with arrival times picked on at least five sensors and located within the cylinder as defined by the piezo-transducers. A grid search algorithm within the InSite software (Itasca; Pettitt and Young, 2007), was used to locate the events, considering a time-dependent transverse isotropic velocity model constrained by the measured axial and radial velocities (Figure 2a). The locations of the detected events are illustrated using 3D visualization of the µ-CT data of the sample post-testing and coloured by test phase (Figure 3). During the consolidation phase, 68 events were detected as the effective isotropic stresses reached 3 MPa. Only a few events were detected during the isotropic cycling stage, located predominantly in proximity to the radial sensors. This was likely due to rearrangement and friction between the large radial transducers and the sample.

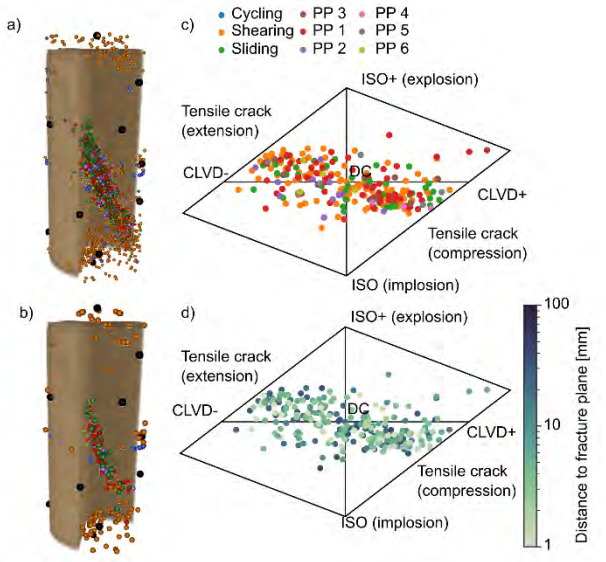


Figure 3. Acoustic emission locations and source mechanisms for Test 1 on the initially intact Castlegate sandstone: a) all AE event locations coloured by test phase (PP: pore pressure reactivation) within a 3D visualization of μ-CT data of the sample post testing. Black spheres give the location of the piezo-transducers for velocity surveys and AE monitoring. b) AE event locations of high SNR events used for moment tensor inversion. (c) and (d) Hudson plots [13] of the decomposition of moment tensors of events in (b) into their isotropic (ISO), double-couple (DC), compensated linear vector dipole (CLVD) by (c) test phase, and (d) by distance to the macroscopic fracture plane.

During the shearing stage, 781 events were detected and located. Events during shearing are initially located near the sample's end surfaces, close to the rock-platens interface. Similar observations were made in [14], and are expected to result from localised frictional slip due to strain incompatibility at the interface between the steel platens and the rock sample ends. In the later stages of shearing, AE events were located towards the centre of the sample, before forming a fracture plane (Figure 3).

For Test 1, the fracture plane formed by the AE events matches the location of the fracture as observed within the μ-CT scan of the sample following the test (Figure 3a; plane with azimuth 286.8 ° and dip 11.14 °). During the stable sliding stage—between the stress drop and unloading to 80 % of the residual strength of the fracture—732 AE events were located. During the six pore pressure pulses, 833, 161, 120, 85, 67 and 57 were located (Figure 3a). Following the formation of the through-going fracture, almost all events were located in close proximity to the fracture.

During Test 2 on the sample containing a clay-filled fracture, only 5 AE events were located within the sample, all occurring during the axial loading phase (Figure 3b). No events were detected during pulse pressure reactivation, and therefore further study of the AE will focus on the results of Test 1.

### *3.2.1 AE characteristics*

Figure 4 shows histograms of the relative magnitudes of AE events during each phase of Test 1 on the clean

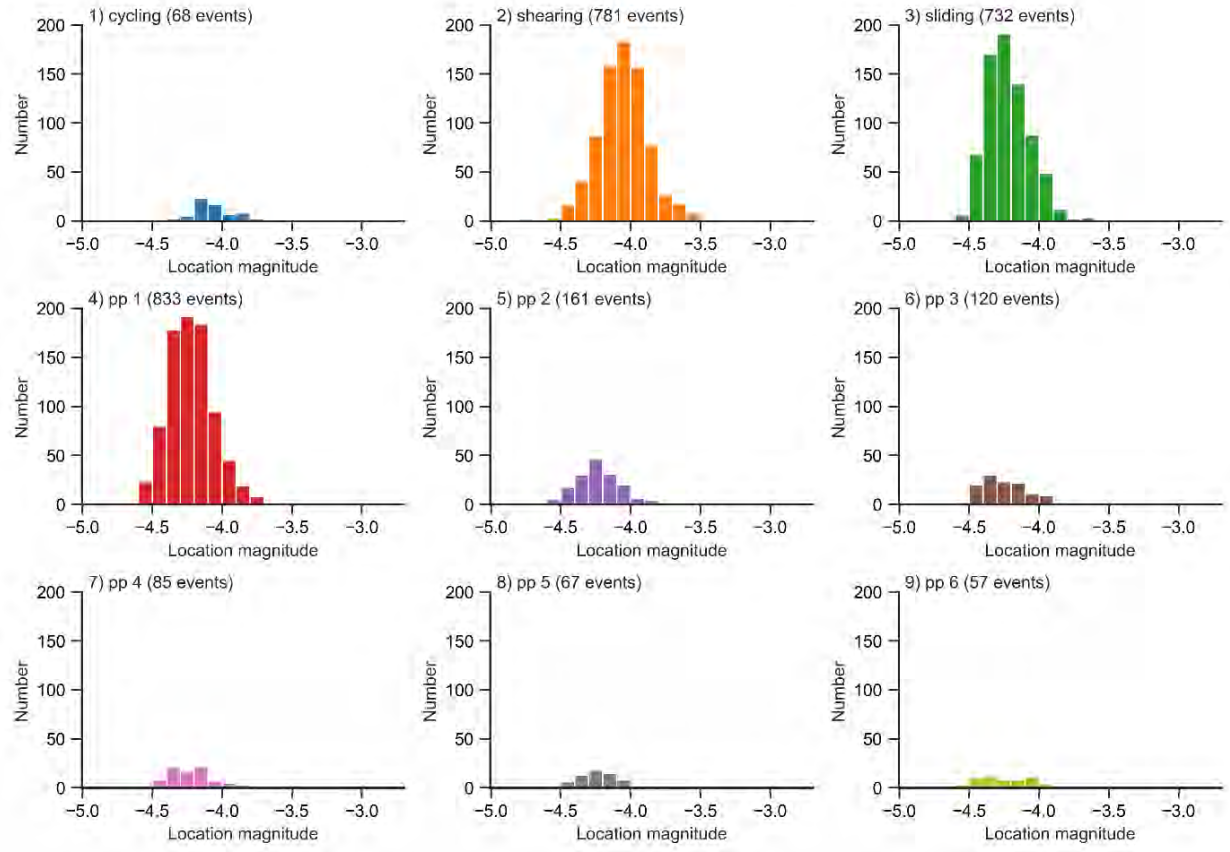


Figure 4. Histograms of the relative magnitudes of AE events during each phase of Test 1 on the clean sandstone (PP: pore pressure reactivation), calculated using Eq. (1).

sandstone, calculated using Eq. (1). The relative magnitudes of events during shearing were overall higher (relative magnitudes centered around -4.0) than during other test phases (relative centered around ~-4.25).

AE can provide insights into fracture source mechanisms by statistical evaluation of P-wave first motion polarities ([15], [16]), or by seismic moment tensor inversion. Moment tensors – a description of the equivalent forces acting at a seismic point source – are commonly inferred from microseismic data and may be decomposed into isotropic, double-couple, and compensated linear vector dipole parts ([17]) and their relative contributions may be analysed ([4], [18]).

Here we selected AE events during Test 1 with P-wave arrival times and amplitudes picked on a minimum of 10 sensors, and with a signal-noise-ratio of the P-wave arrivals of more than 20 for moment tensor inversion. We calculated the moment tensors using a linear inversion of the P-wave amplitudes in the time domain ([12], [19]) considering a homogeneous, time-dependent velocity model updated throughout the experiment from the velocity surveys (Figure 2a). We see that events close to the fracture plane had generally a lower isotropic component than events occurring away from the macroscopic fracture (Figure 3d).

## 4. Discussion

### *4.1 Influence of fault gouge on fault stability*

During the post peak deformation of Test 1, the sample with a clean fracture reached a residual "strength" for stable sliding of the fracture. The sample containing a clay-filled fault, however, became stronger during the axial shearing phase, with no stabilization stress (Figure 2b).

For the clean fracture, we observed a slightly higher pore pressure at reactivation during the very first reactivation phase (3.3 MPa pore pressure; Table 1). For each of the subsequent reactivations of the fracture, including at different rates of pore pressure increase, the reactivation pressure was lower and similar for all (at ~3.1 MPa).

For the sample containing a clay-filled fracture, higher pore pressure increase rates lead to slightly higher reactivation pressures (3.28 MPa at 3 MPa/hr to 3.39 MPa at 24 MPa/hr; Table 1). The pore pressure rate may influence the pore pressure reactivation pressure in presence of the fault gouge, which we attribute to time-dependent, plastic deformation of the clay.

### *4.1 AE response with and without fault gouge*

During Test 1, on the initially intact sample, AE detected during shearing and creation of a through-going fracture were more energetic than during the subsequent fracture reactivation phases (Figure 3). We attribute the higher energy AE to the breaking of cement and grains during the fracturing of the intact sample, releasing more energy than AE resulting from sliding, rolling and fracturing of grains on an already fractured surface.

During each pore pressure reactivation phase of Test 1, the AE events had a similar relative magnitude (Figure 3), and the number of events increased quasi-linearly with strain (Figure 2a), regardless of the pore pressure increase rate.

For the sample containing a clay-filled fracture, we detected very few AE events in comparison, and only during the shearing phase (Figure 2b). The difference in AE response suggests that within the observable frequency range (50 kHz – 1MHz), slip along the clay-filled fracture is aseismic.

### *4.3 Implications for CCS*

These experiments were performed to assess the response of faults to different rates of pore pressure change which may be associated with CCS. While brine was used as the saturating pore fluid, we do not expect our results to strongly differ in presence of $CO_2$ –the presence of $CO_2$ in clay-filled fractures have been shown in the lab to not affect fault stability (e.g. [20]).

Here we see that the laboratory faults are not strongly affected by pore pressurisation rate effects, and it rather is the absolute pressure which governs whether the fault may reactivate. For CCS, $CO_2$ injection rates could potentially be adjusted to avoid unwanted fault reactivation and microseismicity. Our results suggest, however, that the rate of pore pressure change is not expected to induce any change in fault properties – with or without fault gouge. This means that injecting at lower rates may only limit fracture reactivation if it results in lower absolute pore pressures.

We expect rather that fluid mobility and the progression of the pressure front governs where faults and fractures may reactivate. For example, microseismic monitoring at the Decatur $CO_2$ sequestration site has highlighted the significance of hydraulic heterogeneity on $CO_2$ migration, including a hydraulic connection between the reservoir and the basement [21]. Field-scale studies have shown microseismic characteristics—including event magnitude and the size and shape of the microseismic cloud [22], [23]—to be related to the type of fluid injected and its mobility, with fluid viscosity thought to be a key influencing parameter.

## 5 Conclusion

We performed two triaxial tests on a sample of Castlegate sandstone to simulate fault reactivation, whilst measuring axial and radial P-wave velocities and monitoring acoustic emissions. A through-going fracture was created by axial loading, which was then reactivated by pore pressure pulses at rates of 3, 6, 12 and 24 MPa/hr. Following the test, the sample was separated along the fracture plane, and the fracture was filled with a clay (kaolinite) gouge, before being subject to the same test procedure.

For the test on the initially intact rock, AE characteristics (relative magnitudes, locations, source mechanisms) differed between AE events resulting from fracturing and from reactivation of the fracture. AE had similar characteristics for each of the reactivation phases, regardless of pore pressure increase rate. However, for the sample containing a clay-filled fracture, we observed very little AE activity during all test stages.

The pore pressure increase rate had no clear effect on the pressure for reactivation of the clean fracture, i.e. no weakening at higher injection rates. For the sample containing a clay-filled fracture, higher pore pressure increase rates lead to only slightly higher reactivation pressures. These results suggest for the pressurisation rates observed, injection rates may only have a negligible effect on fault stability, which is controlled by the absolute pressure changes.

## Acknowledgements

This work has been produced with support from the SINTEF-coordinated Pre-ACT project (Project No. 271497) funded by the Research Council of Norway RCN, Gassnova (Norway), BEIS (UK), RVO (Netherlands), and BMWi (Germany) and co-funded by the European Commission under the Horizon 2020 program, ACT Grant Agreement No 691712. We also acknowledge the industry partners for their contributions: Total, Equinor, Shell, TAQA. This research was also supported by RCN via CLIMIT grant no. 268520/E20, IGCCS: Induced-seismicity geomechanics for controlled $CO_2$ storage in the North Sea. Additional funding was also given by the European Union's Horizon 2020 research and innovation program under grant agreement number 764531, "SECURe—Subsurface Evaluation of Carbon capture and storage and Unconventional risks".

## References

[1] V. Masson-Delmotte et al., "IPCC, 2018: Summary for Policymakers," 2018.

[2] V. Vilarrasa and J. Rutqvist, "Thermal effects on geologic carbon storage," Earth-science reviews, vol. 165, pp. 245–256, 2017.

[3] M. Rongved and P. Cerasi, "Simulation of stress hysteresis effect on permeability increase risk along a fault," Energies, vol. 12, no. 18, p. 3458, 2019.

[4] E. Aker, D. Kühn, V. Vavryčuk, M. Soldal, and V. Oye, "Experimental investigation of acoustic emissions and their moment tensors in rock during failure," International Journal of Rock Mechanics and Mining Sciences, vol. 70, pp. 286–295, Sep. 2014, doi: 10.1016/j.ijrmms.2014.05.003.

[5] L. Griffiths, O. Lengliné, M. J. Heap, P. Baud, and J. Schmittbuhl, "Thermal Cracking in Westerly Granite Monitored Using Direct Wave Velocity, Coda Wave Interferometry, and Acoustic Emissions," Journal of Geophysical Research: Solid Earth, Mar. 2018, doi: 10.1002/2017JB015191.

[6] P. Baud, E. Klein, and T. Wong, "Compaction localization in porous sandstones: spatial evolution of damage and acoustic emission activity," Journal of Structural Geology, vol. 26, no. 4, pp. 603–624, Apr. 2004, doi: 10.1016/j.jsg.2003.09.002.

[7] M. C. Eppes et al., "Deciphering the role of solar-induced thermal stresses in rock weathering," Geological Society of America Bulletin, vol. 128, no. 9–10, pp. 1315–1338, May 2016, doi: 10.1130/B31422.1.

[8] D. Lockner, "The role of acoustic emission in the study of rock fracture," International Journal of Rock Mechanics and Mining Sciences & Geomechanics Abstracts, vol. 30, no. 7, pp. 883–899, décembre 1993.

[9] D. A. Lockner, J. D. Byerlee, V. Kuksenko, A. Ponomarev, and A. Sidorin, "Quasi-static fault growth and shear fracture energy in granite," Nature, vol. 350, no. 6313, pp. 39–42, Mar. 1991, doi: 10.1038/350039a0.

[10] P. Cerasi, A. Stroisz, E. Sønstebø, S. Stanchits, V. Oye, and R. Bauer, "Experimental investigation of injection pressure effects on fault reactivation for CO2 storage," International Journal of Greenhouse Gas Control, vol. 78, pp. 218–227, Nov. 2018, doi: 10.1016/j.ijggc.2018.08.011.

[11] T. Berre, "Triaxial testing of soft rocks," Geotechnical Testing Journal, vol. 34, no. 1, pp. 61–75, 2010.

[12] W. S. Pettitt and R. P. Young, "InSite seismic processor–user operations manual version 2.14," Applied Seismology Consultants, Shrewsbury, UK, 2007.

[13] J. A. Hudson, R. G. Pearce, and R. M. Rogers, "Source type plot for inversion of the moment tensor," Journal of Geophysical Research, vol. 94, no. B1, p. 765, 1989

[14] L. Griffiths et al., "Inferring microseismic source mechanisms and in situ stresses during triaxial deformation of a North-Sea-analogue sandstone," Advances in Geosciences, vol. 49, pp. 85–93, Sep. 2019, doi: 10.5194/adgeo-49-85-2019.

[15] S. Stanchits, S. Vinciguerra, and G. Dresen, "Ultrasonic velocities, acoustic emission characteristics and crack damage of basalt and granite," Pure and Applied Geophysics, vol. 163, pp. 974–993, 2006

[16] A. Zang, F. Christian Wagner, S. Stanchits, G. Dresen, R. Andresen, and M. A. Haidekker, "Source analysis of acoustic emissions in Aue granite cores under symmetric and asymmetric compressive loads," Geophys J Int, vol. 135, no. 3, pp. 1113–1130, Dec. 1998

[17] L. Knopoff and M. J. Randall, "The compensated linear-vector dipole: A possible mechanism for deep earthquakes," Journal of Geophysical Research (1896-1977), vol. 75, no. 26, pp. 4957–4963, 1970.

[18] G. Kwiatek, T. H. W. Goebel, and G. Dresen, "Seismic moment tensor and b value variations over successive seismic cycles in laboratory stick-slip experiments," Geophys. Res. Lett., vol. 41, no. 16, p. 2014GL060159, Aug. 2014, doi: 10.1002/2014GL060159.

[19] G. De Natale and A. Zollo, "Earthquake focal mechanisms from inversion of first P and S wave motions," in Digital seismology and fine modeling of the lithosphère, Springer, 1989, pp. 399–419.

[20] J. Samuelson and C. J. Spiers, "Fault friction and slip stability not affected by Co2 storage: Evidence from short-term laboratory experiments on North Sea reservoir sandstones and caprocks," International Journal of Greenhouse Gas Control, vol. 11, pp. S78–S90, Nov. 2012, doi: 10.1016/j.ijggc.2012.09.018.

[21] B. P. Goertz-Allmann, S. J. Gibbons, V. Oye, R. Bauer, and R. Will, "Characterization of induced seismicity patterns derived from internal structure in event clusters," Journal of Geophysical Research: Solid Earth, vol. 122, no. 5, pp. 3875–3894, 2017, doi: 10.1002/2016JB013731.

[22] S. J. Ha, J. Choo, and T. S. Yun, "Liquid CO2 Fracturing: Effect of Fluid Permeation on the Breakdown Pressure and Cracking Behavior," Rock Mechanics and Rock Engineering, vol. 51, no. 11, pp. 3407–3420, Nov. 2018, doi: 10.1007/s00603-018-1542-x.

[23] J. P. Verdon, J.-M. Kendall, and S. C. Maxwell, "A comparison of passive seismic monitoring of fracture stimulation from water and C O2 injection," GEOPHYSICS, vol. 75, no. 3, pp. MA1–MA7, May 2010.